Hierarchical nanocomposites with an N-doped carbon shell and bimetal core: novel enzyme nanocarriers for electrochemical pesticide detection

Li Ma, Liya Zhou, Ying He, Lihui Wang, Zhihong Huang, Yanjun Jiang, Jing Gao

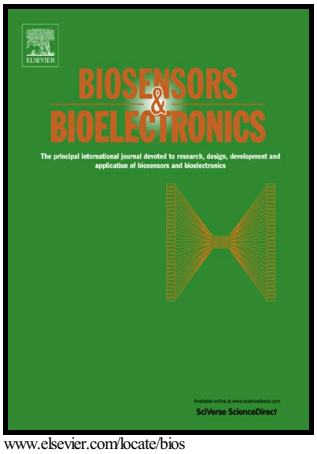

www.elsevier.com/locate/bios

PII: S0956-5663(18)30637-7
DOI: https://doi.org/10.1016/j.bios.2018.08.038
Reference: BIOS10702

To appear in: *Biosensors and Bioelectronic*

Received date: 12 May 2018
Revised date: 19 July 2018
Accepted date: 16 August 2018

Cite this article as: Li Ma, Liya Zhou, Ying He, Lihui Wang, Zhihong Huang, Yanjun Jiang and Jing Gao, Hierarchical nanocomposites with an N-doped carbon shell and bimetal core: novel enzyme nanocarriers for electrochemical pesticide detection, *Biosensors and Bioelectronic,* https://doi.org/10.1016/j.bios.2018.08.038

Hierarchical nanocomposites with an N-doped carbon shell and bimetal core: novel enzyme nanocarriers for electrochemical pesticide detection

Li Ma[a], Liya Zhou[a], Ying He[a], Lihui Wang[a], Zhihong Huang[a], Yanjun Jiang[a] *, Jing Gao[a,b]

[a] School of Chemical Engineering and Technology, Hebei University of Technology, Tianjin 300130, China.

[b] National-Local Joint Engineering Laboratory for Energy Conservation of Chemical Process Integration and Resources Utilization, Hebei University of Technology, Tianjin 300130, China

yanjunjiang@hebut.edu.cn

jgao@hebut.edu.cn

* Corresponding author: Tel: +86-22-60204945; fax: +86-22-60204294

Abstract: Core−shell structured nanocomposites (named PtPd@NCS) with N-doped carbon shell and bimetal core (Pt and Pd) were fabricated through a facile strategy for the first time. The PtPd@NCS nanocomposites were obtained through reduction of K_2PtCl_4, H_2PtCl_6 and Na_2PdCl_4 species, self-polymerization of dopamine (DA) and

co-assembly of Pluronic F127 using a one-pot approach. DA serves as a reductant, as well as a carbon and nitrogen source. The core-shell structure of the PtPd@NCS nanocomposites was characterized and the result indicated that Pt-Pd nanoparticle core with a diameter of approximately 15 nm was encased in the N-doped carbon shells with a thickness of approximately 35 nm. The PtPd@NCS nanocomposites were used as an electrode material to prepare acetylcholinesterase (AChE) biosensors for detecting organophosphate pesticides. The obtained AChE biosensor exhibited a linear range of 1×10^{-14} - 1×10^{-10} M and 1×10^{-9} - 1×10^{-5} M within the detection limit of 7.9×10^{-15} M for malathion, 1×10^{-13} - 1×10^{-6} within the detection limit of 7.1×10^{-14} M for chlopyrifos, and 1×10^{-14} - 1×10^{-11} M and 1×10^{-10} - 1×10^{-5} M within the detection limit of 8.6×10^{-15} M for parathion methyl. The proposed biosensor also exhibited high selectivity, reproducibility and stability. The AChE biosensor was also applied in real samples for detecting organophosphate pesticides and exhibited acceptable recovery. This work demonstrated that the PtPd@NCS had great potential in constructing biosensors to detect organophosphate pesticides and other analytes.

Keywords: Core-shell; Bimetal; N-doped; Dopamine; Biosensor;

1. Introduction

Carbon-based porous materials have attracted extensive attention because of their favourable electrical conductivity, high specific surface area, proper pore size distribution, and stability (Tang et al., 2015). In particular, core-shell carbon structures are presently attracting considerable attention in the research community, as they have great potential for applications in biomedicine, catalysis (Miao et al., 2016; Park & Kim, 2014; Shi et al., 2017; Sun et al., 2016), adsorption/separation (Yamauchi, 2008), and lithium-ion batteries (Qin et al., 2016; Singuru et al., 2017),

etc. Until now, various core-shell nanostructures have been created via different synthesis methods, such as selective etching, microemulsion, spray pyrolysis, bottom-up encapsulation, top-down encapsulation, selective removal, galvanic displacement, or combined strategies (El-Toni et al., 2016; Li & Tang, 2014; Priebe & Fromm, 2015). These methods are multi-step processes, including the pre-synthesized core, growth of a single or hybrid layer, depositing the target shell, and selective etching of the coated layer to form the core-shell nanoparticles. Nevertheless, for the purpose of low environmental pollution and high efficiency, non-sacrificial template methods are more attractive thanks to the simplicity of the preparation procedure and smaller amounts of chemical waste (Do et al., 2017). Non-sacrificial template approaches are mainly based on Ostwald ripening or the Kirkendall process for the synthesis of core-shell nanoparticles (Li & Tang, 2014; Shaik et al., 2017). These methods simplify the process associated with fabricating core-shell nanoparticles, but further research is also necessary. Designing a simple strategy without requiring of any prerequisite conditions for the fabrication of core-shell carbon structures remains a great challenge.

Recent studies have revealed that core-shell metal@carbon nanostructures (such as Ni, Co) can exhibit remarkable electrochemical characteristics and avoid agglomeration (Zhang et al., 2015). The combination of carbon shell and metal core could endow the composite materials with novel properties, rendering them attractive for potential applications in many fields (Zhang et al., 2013; Zhang et al., 2015; Zou et al., 2014). Generally, core-shell metal@carbon nanocomposites are synthesized via the template-assisted selective etching method, which is tedious and time-consuming (Cai, 2015; Liu et al., 2014; Zhang et al., 2018). Recently, much effort has been made to simplify the preparation process. For instance, Su *et al.* prepared Au-cored carbon

spheres by hydrothermal reduction method (Sun & Li, 2004). Xu *et al.* developed a template-free method to synthesize metal@carbon nanospheres through a confined interfacial copolymerization process (Xu et al., 2017). However, template-free methods for core-shell structured materials with a carbon shell and metal core should be further explored. Furthermore, carbon materials are frequently integrated with heteroatoms to form nanocomposites. To our knowledge, nitrogen doping into a carbon matrix has become the most promising method, and nitrogen doping further broadens the applying fields of the carbon materials (Majeed et al., 2013).

Dopamine (DA) can self-polymerize in weak alkaline solutions (Bian et al., 2015), which can be considered as a superb precursor for N-doped carbons. Additionally, the amine and catechol/quinine groups on the ring of DA are good ligands for noble metal ions binding and reduction (Guo et al., 2012; Park & Kim, 2014). DA has often been used for the preparation of N-doped carbon materials (Wang et al., 2017; Zhang et al., 2016). However, DA has never been used as both the reductant and the carbon and nitrogen source needed to synthesize core@shell structured nanocomposites. Furthermore, a one-pot template-free approach for preparing core-shell nanostructure with N-doped carbon shell and metal core has not been explored in detail using dopamine.

Organophosphate (OPs) compounds have been used as pesticides to control various agricultural pests in modern agriculture. However, due to their widespread usage, the persistence of OPs in the environment has caused serious damage to human health and environmental safety. Electrochemical acetylcholinesterase (AChE) based biosensors, which possess the advantages of rapid response and high sensitivity, have shown great potential for rapid OPs detection (Cui et al., 2018; Ding et al., 2014; Santos et al., 2015; Zhao et al., 2015). For further improving the conductivity,

sensitivity and biocompatibility of the biosensors, various of nanomaterials such as Pd@Au nanorods (Lu et al., 2018), graphene quantum dots (Caballero-Díaz et al., 2017), metal-organic frameworks (Liu et al., 2017), interlocked graphene–prussian blue hybrid composites (Zhang et al., 2017) and transition metal nanocomposites (Nasir et al., 2017; Zhou et al., 2017) have been used to prepare novel biosensors. In addition, prussian blue (Zhao et al., 2015), 7,7,8,8- tetracyanoquinodimethane (TCNQ) (Rotariu et al., 2012) and cobalt phthalocyanine (Moraes et al., 2009; Yoon et al., 2014) have been used to decrease the working potential of biosensors. Although many nanomaterials modified AChE biosensors have been prepared, their applications in pesticides detection in real samples are still at the early stage. Therefore, developing novel functionalized nanomaterial with improved stability and favorable biocompatibility to immobilize AChE to construct biosensors is still needed.

Thus, in this work, Pt-Pd nanoparticles encapsulated in N-doped carbon shells (PtPd@NCS) with an elegant core-shell nanostructure were synthesized via an in situ hydrothermal reaction followed by heat treatment in a nitrogen atmosphere. The morphology, structure and composition of the obtained PtPd@NCS were characterized. To the best of our knowledge, this is the first study of the one-pot preparation of core-shell structured nanocomposites with an N-doped carbon shell and bimetal core. The obtained PtPd@NCS was used to construct AChE biosensors for OPs detection in real samples. The interference study was also conducted to assay the selectivity of the AChE biosensors.

2. Experimental section

2.1 Chemicals

Acetylthiocholine chloride (ATCl), chitosan (CS, Mw=15000, deacetylation 95%), dopamine hydrochloride, sodium tetrachloropalladate (Na_2PdCl_4), potassium

tetrachloroplatinate (K_2PtCl_4), chloroplatinic acid hexahydrate ($H_2PtCl_6 \cdot 6H_2O$), Pt/C catalyst (20% Pt), $K_3Fe(CN)_6$, malathion, methyl parathion and chlopyrifos were purchased from Aladdin (Shanghai, China). Acetylcholinesterase (AChE, E.C.3.1.1.7, 200-1000 units/mg protein) and Pluronic F127 were purchased from Sigma-Aldrich (Beijing, China). All the chemical reagents used in this study were of analytical grade.

2.2 Apparatus

SEM was conducted on a JEOL JSM-6700F scanning electron microscope. TEM observations were carried out on an FEI Tecnai G2 and F20 microscopes at 200 kV and equipped for energy-dispersive spectrometer (EDS) analysis. XRD data were obtained with Cu Kα (λ = 1.5418 Å) radiation operating at 40 kV, 40 mA and a scanning rate of 8° min^{-1} with a narrow receiving slit (0.6) on a Bruker D8 Discover. Raman spectra analysis was performed on a Renishaw in Via Reflex confocal Raman microscope at 532 nm. XPS investigation was conducted on a Thermo Scientific Escalab 250Xi system using an Al Kα anode.

The electrochemical measurements were conducted on a CHI650E electrochemical work station (Shanghai, China). All the experiments were performed using a conventional three-electrode electrochemical system. A saturated calomel electrode was used as the reference electrode. Pt foil and glassy carbon electrode (GCE) were used as the counter electrode and working electrode, respectively.

2.3 Synthesis of the PtPd@NCS

Briefly, the aqueous solutions of K_2PtCl_4 (1.2 mL, 20 mM), H_2PtCl_6 (1.8 mL, 20 mM), Na_2PdCl_4 (0.6 mL, 20 mM) and 40 mg of Pluronic F127 were ultrasonically mixed. After adding 6.0 mL of the dopamine hydrochloride solution (20 mM), the mixture was continuously stirred for 12 h at 70°C. The produced precipitate was separated by centrifugation (10000 rpm, 10 min) and washed with water and ethanol for three times

to remove the residual F127. The products named PtPd@PDA were obtained after drying at room temperature. For carbonization, the PtPd@PDA samples were heated at 1°C min^{-1} from room temperature to 350°C and kept at 350°C for 3 h in a nitrogen atmosphere. The temperature was then increased at a rate of 1°C min^{-1} to 800°C and kept for 2 h. Finally, the PtPd@NCS was obtained.

In addition, the synthesis process of mesoporous PtPd nanosphere (MPtPdN) and mesoporous carbon sphere (MCS) is shown in Supporting Information.

2.4 Preparation of PtPd@NCS modified electrodes

The GCE with a diameter of 3 mm was first cleaned with alumina slurry and then ultrasonicated with ethanol, nitric acid solution (v/v, 1:1) and DI water.

Typically, 1.0 mg of PtPd@NCS was added into 2.0 mL of 0.2 % CS solution and ultrasonicated until a homogeneous suspension of CS-PtPd@NCS was obtained. An aliquot (6 μL) of the CS-PtPd@NCS suspension was casted on the surface of a pretreated GCE and then dried in the air (referred to as PtPd@NCS/GCE). Then, the PtPd@NCS/GCE was coated with 6 μL of AChE solution and dried at 4°C. The obtained electrode (referred to as AChE/PtPd@NCS/GCE) was kept at 4°C. To compare the performance of the different modified electrodes, the MPtPdN/GCE, MCS/GCE and Pt/C/GCE were also prepared.

2.5 Electrochemical Measurements

The electrochemical characterization of the stepwise modified electrodes were performed in the presence of 5.0 mM $K_3Fe(CN)_6$ and 0.1 M KCl in 0.1 M PBS (pH 7.5) by cyclic voltammetry (CV) and electrochemical impedance spectroscopy (EIS) method.

The affinity of AChE on the PtPd@NCS to ATCl was investigated by the current-time plot at 650 mV after successive injections of ATCl to PBS (0.1 M, pH

7.5) under stirring condition.

2.6 Measurement procedure

The proposed AChE/PtPd@NCS/GCE biosensor was used to detect pesticides by the differential pulse voltammetry (DPV) method over a potential range of 0.2 - 1.0 V. The obtained AChE/PtPd@NCS/GCE biosensor was first tested for its DPV response in PBS (pH 7.5) containing ATCl (2.0 mM). The original DPV signal was recorded as I_0 and then the biosensor was incubated in different concentrations of malathion solutions. Finally, the biosensor was washed with PBS and then transferred into the ATCl solution (2.0 mM) for DPV measurements. The residual signal was recorded as I_1. The inhibition rate was defined by the following equation:

$$Inhibition\ (\%) = \frac{I_0 - I_1}{I_0} \times 100\%. \quad \text{(Eq.1)}$$

3. Results and discussion

3.1 Synthesis and characterization of PtPd@PDA and PtPd@NCS

Typically, F127 was first mixed with an aqueous solution containing K_2PtCl_4, H_2PtCl_6 and Na_2PdCl_4, so that the dissolved metal ions (Pt^{4+}, Pt^{2+} and Pd^{2+}) interacted with the ethylene oxide groups of the F127. When dopamine hydrochloride (DA) was added, the catechol and amine groups of the DA species and the F127 self-organized into spherical micelles to reduce the interfacial free energy (Guan et al., 2016; Sun et al., 2016). Meanwhile, the metal ions (Pt^{4+}, Pt^{2+} and Pd^{2+}) were reduced to metal nanoparticles, and were encased in the polymerized DA (denoted as PDA) with the block copolymer F127. After the completion of reaction and the removal of F127, the product (denoted as PtPd@PDA) was formed. After heat treatment, the PDA shell was converted to N-doped carbon shell and then the PtPd@NCS was formed. The formation mechanism and process of core-shell structured PtPd@NCS were proposed and described in Scheme 1.

During the synthesis of PtPd@PDA nanospheres, the amount of dopamine hydrochloride was optimized (Fig. S1). As shown in Fig. S1, when 15 mM of DA was used, the PtPd@PDA varied greatly in size. Further increasing the amount of DA to 25 mM, highly dispersed nanospheres with a mesoporous structure were obtained. This can be ascribed to the usage of the appropriate concentration of dopamine hydrochloride that can control the nanosphere's growth rate and polymerization speed. Further increasing the concentration of DA to 30 mM, the PtPd@PDA nanocomposites stick together due to the excess DA polymerization in the reaction system. Thus, the PtPd@PDA spheres were prepared using a 25 mM DA solution in the subsequent experiments.

As shown in Fig. 1a, these PtPd@PDA nanospheres are fairly uniform in shape with a size of approximately 85 nm. Well-defined mesopores, which were induced by the F127, are well distributed over the PtPd@PDA nanosphere's surface. As can be seen from Fig. 1b, the PtPd@PDA are nanospheres with core-shell structures, and Pt and Pd nanoparticles are encapsulated in a PDA shell with a thickness of approximately 30 nm. The elemental mapping analysis showed that the C and N elements enriched in the shell, while Pt and Pd elements were concentrated in the interior of the PtPd@PDA spheres (Fig. S2). After heat treatment in a nitrogen atmosphere, the PtPd@PDA nanospheres were converted to PtPd@NCS. The SEM and TEM images of PtPd@NCS showed that the spherical morphology and core-shell structure were retained (Fig. 1c and 1d). The loosen shell structure of the PtPd@NCS can be attributed to the generation of gas in calcination process, which is similar with literatures' results (Wang et al., 2017; Tang et al., 2015). The selected-area electron diffraction pattern (Fig. 1e) shows ring patterns with intense spots that could be assigned to the (111), (200), (220), and (311) planes of Pt and Pd face-centred-cubic

(fcc) crystals (Jiang et al., 2016). The C, N, Pt and Pd elements were completely retained in PtPd@NCS after heat treatment, which was further confirmed by the elemental mapping analysis (Fig. 1f). The images showed that the C, N, Pt and Pd elements were homogenously distributed within the PtPd@NCS. The N-doped carbon shell can prevent the "entrapping" of Pt and Pd nanoparticles from coalescence and dissolution, and the synergetic effect between the noble metal nanoparticles and the nitrogen-doped carbon is beneficial for potential catalytic and electrochemical applications.

The chemical compositions of the PtPd@PDA and PtPd@NCS were analysed by XRD and these results are shown in Fig. 2a. The 2θ values of 39.77°, 46.23°, 67.45°, 81.28°, and 85.92° were indexed as the (111), (200), (220), (311), and (222) planes of the fcc crystal structure, respectively, which are consistent with the Pt (JCPDS88-2335) and Pd (JCPDS01-1190) XRD results. However, in the wide-angle XRD patterns, it is difficult to resolve Pt and Pd crystals because the lattice mismatch ratio of Pt/Pd is 0.77% (Jiang et al., 2015).

The high degree graphitization in PtPd@NCS is further confirmed by Raman spectroscopy. As shown in Fig. 2b, there are two characteristic bands in the Raman spectra for PtPd@PDA. One is the D band (disordered carbon) at 1340 cm^{-1} and the other is G band (graphitic carbon) at 1598 cm^{-1}. The intensity of the G band for PtPd@NCS is much higher than for PtPd@PDA, which is indicative of its highly graphitic character. The weak D band of the PtPd@NCS implied the introduction of defects by N-doping during the graphitization of PDA. The graphitic carbon in the PtPd@NCS samples will enhance electron transport (Wang et al., 2015; Wang et al., 2016).

XPS was employed to confirm the elemental compositions of the PtPd@PDA and

PtPd@NCS. As shown in Fig. 3a, the presence of C, O, N, Pt, and Pd species on the PtPd@PDA and PtPd@NCS was confirmed. Table S1 gives the surface element composition of the PtPd@PDA and PtPd@NCS. As shown in Fig. 3b, the N1s spectrum of the PtPd@PDA exhibits one peak centred at 399.8 eV, which is assigned to the pyrrole N in the amine groups of the PDA (Miao et al., 2016; Sun et al., 2016). After carbonization, the N1s spectrum of the PtPd@NCS is deconvoluted into two peaks, including the pyridinic N (400.8 eV) and graphitic N (398.9 eV) peaks. The co-existence of pyridinic N and graphitic N may be interpreted as doped nitrogen in the PtPd@NCS. The C1s species of the PtPd@PDA and PtPd@NCS were also investigated (Fig. 3c). The C1s core level peak of the PtPd@PDA has the following five main peaks: C-C (284.6 eV), C-N (285.7 eV), C-OH (286.5 eV), C=O (286.8 eV), and O-C=OH (289.0 eV). These peaks are ascribed to the indole ring in the PDA (Park & Kim, 2014; Shi et al., 2017). For the PtPd@NCS samples, the increased intensity of 284.6 eV is related to the C-C bond.

To gain clear insight into the state of the metal NPs in the PtPd@NCS, XPS analysis on the Pt4f binding energy was conducted. As can be seen in Fig. 3d, two sets of spin-orbit doublets are recognized from the Pt ($4f_{5/2, 7/2}$). The peaks at 71.4 and 74.7 eV were assigned to the Pt (0) species in the PtPd@NCS. The binding energy values at 71.8 and 76.0 eV were ascribed to the Pt (Ⅱ) species (Qin et al., 2016; Song et al., 2016). Similarly, the high resolution Pd3d scan (Fig. 3e) displayed two states of the Pd in the PtPd@NCS as follows: one was a Pd (0) dominated with two peaks at 335.3 eV and 336.1eV, and the other was Pd (Ⅱ) dominated with double binding energies of 340.9 eV and 341.6 eV (Singuru et al., 2017).

3.2 Electrochemical properties of the modified electrodes

The as-prepared PtPd@NCS with a core@shell nanostructure exhibited unique

electronic properties and may find applications in the fabrication of biosensors. Thus, to evaluate the electrochemical activity, the PtPd@NCS was used to construct AChE biosensors to detect OPs. For comparison, mesoporous bimetallic PtPd nanoflowers (MPtPdN), mesoporous cabon sphere (MCS) and Pt/C particles were also used to prepare biosensors under the same conditions.

In a typical experiment, the same amount of PtPd@NCS, MPtPdN, MCS and Pt/C were loaded onto the GCE, respectively, and CV was performed to evaluate the charge transfer process at the surface of the modified electrodes. Fig. 4a shows the CV curves of the different modified electrodes in $K_3Fe(CN)_6$ and KCl mixed solution. The CV curve of the PtPd@NCS/GCE electrode displayed an enhanced current with a pair of well-defined redox peaks contrasted with MPtPdN, MCS and Pt/C modified electrodes. In addition, EIS was used to study the interface properties of the modified electrode. Electronic transfer resistance (R_{et}) was also evaluated. As shown in Fig. 4b, compared to bare GCE, MPtPdN/GCE, MCS/GCE and Pt/C/GCE, PtPd@NCS/GCE exhibited smaller semicircular domains. The EIS results further confirmed that PtPd@NCS displayed superior electrochemical performance. The remarkable property may be ascribed to the synergetic effect of N-doped carbon shell and noble metal core that facilitated charge transfer. The N atoms can activate a large number of adjacent C atoms and promote the electron transfer (Tang et al., 2015). Furthermore, the Gibbs free energy of the electronic transfer can be reduced due to the d-oribital coupling effect between the fully occupied (Pt) and lower occupancy (Pd) of d-oribital metals (Xue et al., 2016). Thus, incorporation of various dopants into PtPd@NCS provided sufficient electronic conductive channels. Base on the above results, PtPd@NCS was chosen as the modified material of electrode to be studied in detail.

The CV curves of the bare GCE, PtPd@NCS/GCE and AChE/PtPd@NCS/GCE were

also investigated in 0.1 M PBS (pH 7.5) solution containing 1.0 mM of ATCl, and these results are shown in Fig. 4c. There is no peak observed for the bare GCE and PtPd@NCS/GCE. In contrast, an obvious irreversible oxidation peak can be observed for the AChE/PtPd@NCS/GCE. This oxidation peak is corresponded to the oxidation of thiocholine(the hydrolysis product of ATCl catalysed by AChE) (Deng et al., 2016; Ju et al., 2015).

3.3 Amperometric response to ATCl

Fig. 5 shows the amperometric curve at the AChE/PtPd@NCS/GCE electrode on successive injections of ATCl. The inset of Fig. 5 shows the calibration plots to the concentration of ATCl and response current of the AChE/PtPd@NCS/GCE electrode. The linear working ranges were 25 – 325 μM and 425 – 1925 μM with linear regression equations of I (μA) = 0.00225 C (μM) + 0.1057 (R^2=0.9935) and I (μA) =0.0008978 C (μM) + 0.5641 (R^2=0.9905), respectively. The current reached a stable value within 5 s after each addition, indicating the excellent sensitivity of the AChE/PtPd@NCS/GCE. When the ATCl concentration was higher than 1925 μM, the amperometric response was stable, showing the characteristics of the Michaelis-Menten kinetic mechanism. The value of apparent Michaelis–Menten constant (K_m) was 0.695 mM (Supporting Information). The Km value of the AChE/PtPd@NCS/GCE was lower than that of the PAMAM-G4 dendrimer (Santos et al, 2015), the conducting polymer and carbon nanotubes modified electrodes (Kesik et al., 2014), indicating good affinity and enzymatic activity of the AChE to the substrate.

3.4 Pesticide detection

The influences of the pH of the supporting electrolyte, the concentration of ATCl, concentration of the AChE and the inhibition time for the malathion on the biosensor

performance were investigated. Based on the results shown in Fig. S3, the PBS with pH 7.5, 2.0 mM of ATCl, 0.10 U of AChE and a 600 s inhibition time were selected as the optimal conditions for the following experiments. Under the optimal condition, the AChE/PtPd@NCS/GCE biosensor was used for malathion determination by DPV, with the sensitivity of the biosensor evaluated after inhibition via a series of malathion concentrations (Fig. 6). The DPV response of the AChE/PtPd@NCS/GCE exhibited an obvious oxidation peak at approximately 650 mV. The peak current decreased with the increase in concentration of malathion, which was associated with the inhibition of AChE activity by malathion. The decrease in the oxidation peak current occurred as a result of blocking serine hydroxyl groups of the AChE covalently bound to the pesticides, which decreased the activity of AChE (Songa & Okonkwo, 2016; Wei & Wang, 2015). As shown in Fig. 6b, the linear ranges are 1×10^{-14} - 1×10^{-10} M and 1×10^{-9} - 1×10^{-5} M with a detection limit of 7.9×10^{-15} M (S/N=3). Permissible limits of malathion residues in potato and corn grain samples are 3.0×10^{-6} and 2.4×10^{-5} M (United States of America Environmental Protection Agency 2014), respectively. The prepared AChE/ PtPd@NCS/GCE biosensor in this work is able to detect as much as 10^{-15} M. The AChE/ PtPd@NCS/GCE biosensor was further used in the detection of parathion methyl and chlopyrifos (Fig. S5, S6), and these results are summarized in Table 1. Compared to other reported AChE biosensors (Table 2), the prepared AChE/PtPd@NCS/GCE biosensor exhibited a lower detection limit and a wider linear range. Thus, the superior performance of the AChE/PtPd@NCS/GCE biosensor is believed to originate from the structure and unique composition of the PtPd@NCS. First, both the core-shell architecture and porous structure can increase the specific surface area, warrant fast diffusion of the substrates and products, and facilitate the electron transfer rate. Second, the N-doped carbon shell not only improves the

conductivity of the electrode materials, but also prevents the metal nanoparticles from self-agglomeration. Third, the synergistic effect of the N-doped carbon, Pt, and Pd species can also contribute to the enhanced electrochemical performance.

3.5 Interference study

The DPV response of the AChE/PtPd@NCS/GCE biosensor incubated in 1×10^{-10} M malathion was studied in the absence and presence of interfering species. As shown in Fig. S7, no significant changes in the current response are observed in the presence of Cu^{2+}, Mg^{2+}, Fe^{2+} SO_4^{2-}, PO_4^{3-}, NO_3^-, glucose, and citric acid in the DPV response, indicating the good selectivity of the biosensor. An interference study with other pesticides, such as chlorpyrifos and carbaryl, was also investigated. These results showed that equal concentrations of these pesticides interfered with each other for determination. In contrast, chlordane, one of the non-organophosphates had no influence on the detection of malathion.

3.6 Precision of measurements, stability and real samples analysis

Inter-assay precision measurements were carried out by testing eight different electrodes in 1.0 mM of ATCl after being treated with 1×10^{-10} M malathion for 600 s. The intra-assay precision was evaluated using one prepared electrode with eight repeated determinations. The calculated RSD values for the intra- and inter-assay were 2.34% and 3.31%, respectively, demonstrating the good repeatability and reproducibility of the proposed electrode. In addition, the biosensor retained 91.62% of the initial current response after storage at 4 °C for 30 days, suggesting good storage properties for the AChE/PtPd@NCS/GCE electrode. The application of the proposed AChE/PtPd@NCS/GCE biosensor was evaluated using the spiked cabbage samples containing different concentrations of malathion, parathion methyl and chlopyrifos. Table S2 demonstrates that the proposed biosensor can be successfully

applied in determining pesticides in cabbage and an acceptable recovery of 93.21 - 104.3% is obtained.

4 Conclusions

A versatile and facile approach to fabricating core@shell structured nanocomposites with an N-doped carbon shell and a bimetal core was developed for the first time using dopamine as the reductant and carbon and nitrogen sources. The well-defined core-shell nanostructure, noble metal core, pyridinic N doped carbon shell, as well as the synergetic couplings, endowed the PtPd@NCS with high electrochemical activity. When PtPd@NCS was used to modify a glassy carbon electrode, the obtained AChE biosensor exhibited a high electrochemical response, and a low limit of detection. The stable and sensitive AChE/PtPd@NCS/GCE biosensor may provide an efficient strategy for detecting organophosphate pesticides. Overall, this work developed a novel platform for preparing core-shell structured nanocomposites and their derived materials with tailored morphology and graphitization, which may find applications in biosensors, catalysis and nanomedicine.

Acknowledgments

This work was supported by the National Nature Science Foundation of China (Nos. 21576068, 21276060, 21276062, and 21306039), the Natural Science Foundation of Tianjin, China (16JCYBJC19 800), the Natural Science Foundation of Hebei Province, China (B2015202082, B2016202027, and B2017202056), the Program for Top 100 Innovative Talents in Colleges and Universities of Hebei Province, China (SLRC2017029) and Hebei High level personnel of support program, China (A2016002027).

References

Bian, S.W., Liu, S., Chang, L. 2015. J. Mater. Sci., 51, 3643-3649.

Caballero-Díaz, E., Benítez-Martínez, S., Valcárcel, M. 2017. Sensor Actuat. B-Chem., 240, 90-99.

Cai, Z., Xu, L., Yan, M., Han, C., He, L., Hercule, K. M., Chaojiang Niu,C., Yuan, Z., Xu, W., Qu, L., Zhao, K.,and Liqiang Mai, L. 2015. Nano. Lett., 15, 738-761.

Chauhan, N., Narang, J., Pundir, C.S. 2011. Biosens. Bioelectron., 29, 82-88.

Chauhan, N., Pundir, C.S. 2012. Electrochim. Acta, 67, 79-86.

Cui, H. F., Wu, W.W., Li, M.M., Song, X.J., Lv, Y.X., Zhang, T.T. 2018. Biosens. Bioelectron., 99, 223-229.

Deng, Y., Liu, K., Liu, Y., Dong, H., Li, S. 2016. J. Nanosci. Nanotechnol., 16, 9460-9467.

Ding, J., Zhang, H., Jia, F., Qin, W., Du, D. 2014. Sensor. Actuat. B-Chem., 199, 284-290.

Do, Q.C., Kim, D.G., Ko, S.O. 2017. ACS Appl. Mater. Inter., 9, 28508-28518.

Du, D., Wang, M., Cai, J., Qin, Y., Zhang, A. 2010. Sensors Actuat. B-Chem., 143, 524-529.

Ebrahim, S., El-Raey, R., Hefnawy, A., Ibrahim, H., Soliman, M., Abdel-Fattah, T.M. 2014. Synthetic Metals, 190, 13-19.

El-Toni, A.M., Habila, M.A., Labis, J.P., ZA, A.L., Alhoshan, M., Elzatahry, A.A., Zhang, F. 2016. Nanoscale, 8, 2510-2531.

Guan, B.Y., Yu, L., Lou, X.W. 2016. Adv. Mater., 28, 9596-9601.

Guo, L., Liu, Q., Li, G., Shi, J., Liu, J., Wang, T., Jiang, G. 2012. Nanoscale, 4, 5864-5867.

Jiang, B., Li, C., Imura, M., Tang, J., Yamauchi, Y. 2015. Adv. Sci., 2, 1500112.

Jiang, B., Li, C., Malgras, V., Imura, M., Tominaka, S., Yamauchi, Y. 2016. Chem. Sci., 7, 1575-1581.

Ju, K., Feng, J., Feng, J., Zhang, Q., Xu, T.,Wei, J. 2015. Microchim. Acta, 182, 2427-2434.

Kaur, N., Thakur, H., Prabhakar, N. 2016. J.Electroanal. Chem., 775, 121-128.

Kesik, M., Ekiz Kanik, F., Turan, J., Kolb, M., Timur, S., Bahadir, M., Toppare, L. 2014. Sensors Actuat. B-Chem., 205, 39-49.

Li, G., Tang, Z. 2014. Nanoscale, 6, 3995-4011.

Liu, C.S., Sun, C.X., Tian, J.Y., Wang, Z.W., Ji, H.F., Song, Y.P., Zhang, S., Zhang, Z.H., He, L.H., Du, M. 2017. Biosens. Bioelectron., 91, 804-810.

Liu, R., Qu, F., Guo, Y., Yao, N., Priestley, R.D. 2014. Chem. Commun., 50, 478-480.

Lu, X., Tao, L., Song, D., Li, Y., Gao, F. 2018. Sensors Actuat. B-Chem., 255, 2575-2581.

Majeed, S., Zhao, J., Zhang, L., Anjum, S., Liu, Z., Xu, G. 2013. Nanotechnol. Rev., 2, 615-636.

Miao, J., Liu, H., Li, W., Zhang, X. 2016. Langmuir, 32, 5365-5372.

Moraes, F.C., Mascaro, L.H., Machado, S.A.S., Brett, C.M.A. 2009. Talanta ,79, 1406-1411.

Nasir, M.Z.M., Mayorga-Martinez, C.C., Sofer, Z., Pumera, M. 2017. ACS Nano, 11, 5774-5784.

Park, J., Kim, S. 2014. J.Electrochem. Soc., 161, 518-524.

Priebe, M., Fromm, K.M. 2015. Chemistry, 21, 3854-3874.

Qin, Y., Chao, L., Yuan, J., Liu, Y., Chu, F., Kong, Y., Tao, Y., Liu, M. 2016. Chem. Commun., 52, 382-385.

Rotariu, L., Zamfir, L.G., Bala, C. 2012. Anal. Chim. Acta, 748, 81–88.

Santos, C. S., Mossanha, R., Pessôa, C. A. 2015, 45(4):325-334. 2015. J. Appl. Electrochem., 45, 325-334.

Shaik, F., Zhang, W., Niu, W. 2017. Langmuir, 33, 3281-3286.

Shi, Q., Zhu, C., Engelhard, M.H., Du, D., Lin, Y. 2017. RSC Adv., 7, 6303-6308.

Singuru, R., Dhanalaxmi, K., Shit, S.C., Reddy, B.M., Mondal, J. 2017. Chem. Cat. Chem., 9, 2550-2564.

Song, C., Park,S.J., Kim, S. 2016. J. Electrochem. Soc., 163, 668-373.

Song, D., Li, Y., Lu, X., Sun, M., Liu, H., Yu, G., Gao, F. 2017. Anal. Chim. Acta., 982, 168-175.

Songa, E.A., Okonkwo, J.O. 2016. Talanta, 155, 289-304.

Sun, T., Li, Z., Wang, H., Bao, D., Meng, F., Zhang, X. 2016. Angew. Chem. Int. Ed., 55, 10662-10666.

Sun, X., Li, Y. 2004. Angew. Chem. Int. Ed., 43, 597-601.

Tang, J., Liu, J., Li, C., Li, Y., Tade, M.O., Dai, S., Yamauchi, Y. 2015. Angew. Chem. Int. Ed., 54, 588-593.

Wang, S., Zhao, Z., Xu, H., Deng, Y., Li, Z., Chen, G. 2015. Electrochim. Acta, 173, 282-289.

Wang, Y., Dong, S., Wu, X., Liu, X., Li, M. 2017. J. Mater.Sci., 52, 9673-9682.

Wang, Z., Li, B., Ge, X., Goh, F.W., Zhang, X., Du, G., Wuu, D., Liu, Z., Andy Hor, T.S., Zhang, H., Zong, Y. 2016. Small, 12, 2580-2587.

Wei, M., Wang, J. 2015. Sensors Actuat. B-Chem., 211, 290-296.

Xu, F., Lu, Y., Ma, J., Huang, Z., Su, Q., Fu, R., Wu, D. 2017. Chem. Commun., 53, 12136-12139.

Xue, H., Tang, J., Gong, H., Guo, H., Fan, X., Wang, T., He, J., Yamauchi, Y. 2016. ACS Appl Mater Interfaces, 8, 20766-207671.

Yamauchi, Y., Takai, A., Nagaura, T., Inoue, S., Kuroda, K. . 2008. J Am Chem Soc, 130, 5426-5427.

Yoon, Y. J., Li, K. H. H., Low, Y. Z., Yoon, J., Ng, S. H. 2014. Sensors Actuat. B-Chem., 198, 233-238.

Zhai, C., Sun, X., Zhao, W., Gong, Z., Wang, X. 2013. Biosens. Bioelectron., 42, 124-130.

Zhang, J., Guo, S., Wei, J., Xu, Q., Yan, W., Fu, J., Wang, S., Cao, M., Chen, Z. 2013. Chemistry, 19, 16087-16092.

Zhang, M., Hou, C., Halder, A., Ulstrup, J, Chi, Q. 2017. Biosens. Bioelectron., 89, 570-577.

Zhang, X., Yan, W., Zhang, J., Li, Y., Tang, W., Xu, Q. 2015. RSC Adv., 5, 65532-65539.

Zhang, Y., Sun, K., Liang, Z., Wang, Y., Ling, L. 2018. Appl. Surf. Sci., 427, 823-829.

Zhang, Y., Zhang, M., Ding, L., Wang, Y., Xu, J. 2016. Nanoscale Res. Lett., 11, 212-218.

Zhao, H., Ji, X., Wang, B., Wang, N., Li, X., Ni, R., Ren, J. 2015. Biosens. Bioelectron., 65, 23-30.

Zhou, L., Zhang, X., Ma, L., Gao, J., Jiang, Y. 2017. Biochem. Eng. J, 128, 243-249.

Zou, X., Huang, X., Goswami, A., Silva, R., Sathe, B.R., Mikmekova, E., Asefa, T. 2014. Angew. Chem. Int. Ed., 53, 4372-4376.

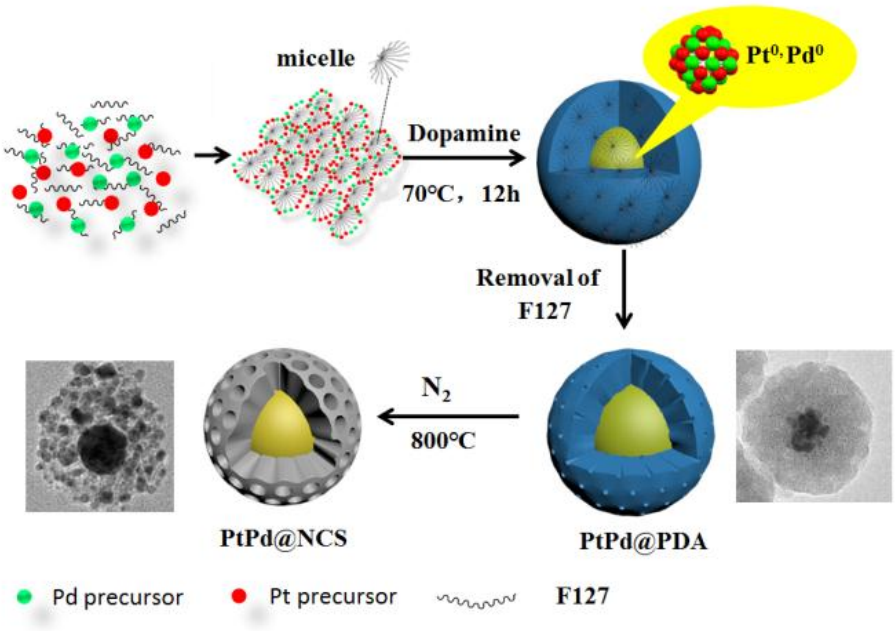

Scheme 1 Formation mechanism and process of the PtPd@NCS

Table 1 Detection of parathion methyl and chlopyrifos with the AChE/PtPd@NCS/GCE

Pesticides	Linear range (M)	Equation of linear regression	Correlation coefficient	RSD	Detection limit (M)
parathion methyl	1×10^{-14}-1×10^{-11}; 1×10^{-10}-1×10^{-5}	I=3.207 lgC +26.43; I=10.35 lgC +41.73	0.9949; 0.9877	4.32; 5.24	8.6×10^{-15}
chlopyrifos	1×10^{-13}-1×10^{-6}	I=7.604 lgC +47.35	0.9935	3.31	7.1×10^{-14}

Table 2 Comparison of the analytical characteristics of the AChE electrochemical biosensors for malathion detection

Modified electrode	Linear range (M)	Detection limit (M)	Ref.
AChE/PEDOT-MWCNTs/FTO	1×10^{-11}–1×10^{-9}	1×10^{-11}	(Kaur et al., 2016;)
AChE-Chitosan/Pd-Cu NWs/GCE	1.5×10^{-13}-3×10^{-9} and	4.5×10^{-9}	(Song et al., 2017)

	1.5×10^{-9}-9×10^{-9}		
PANI-ES–SWCNTs graphite composite electrode	2×10^{-7} -14×10^{-7}	2.0×10^{-7}	(Ebrahim et al., 2014)
CS/AChE/PB-CS/ERGO-AuNPs-β-CD/GCE	2.4×10^{-11}-6×10^{-9} and 1.3×10^{-11}-3×10^{-9}	2.4×10^{-11}	(Zhao et al., 2015)
AChE-MWCNTs-Au-CHIT/GCE	3×10^{-9}-3×10^{-6} and 6×10^{-6}-4.5×10^{-5}	1.8×10^{-10}	(Du et al., 2010)
AchE/MWCNT/CA/NPG	3×10^{-9}–1.5×10^{-7}	1.5×10^{-9}	(Ding et al., 2014)
AChE-Fe_3O_4NPs/c-MWCNTs/ITO	1×10^{-10}–4×10^{-8}	1×10^{-10}	(Chauhan & Pundir, 2012)
AChE/Pin5COOH/ZnS/Au	1×10^{-10}–5×10^{-8}	1×10^{-10}	(Chauhan et al., 2011)
Nafion/AChE/Chit–PB–MWNTs–HGNs/Au	5×10^{-11}–7.5×10^{-8}	5×10^{-11}	(Zhai et al., 2013)
AChE/ PtPd@NCS/GCE	1×10^{-14}-1×10^{-10} and 1×10^{-9}-1×10^{-5}	7.9×10^{-15}	This work

Figure captions

Fig. 1 **a)** SEM, **b)** TEM images of the PtPd@PDA, **c)** SEM, **d)** TEM images of the PtPd@NCS , **e)** selected-areas for electron diffraction (SAED) patterns of a signal from the PtPd@NCS and **f)** elemental mapping of the PtPd@NCS

Fig. 2 **a)** Wide-angle XRD patterns and **b)** Raman spectra of the PtPd@PDA and PtPd@NCS

Fig. 3 **a)** XPS spectra of the PtPd@PDA and PtPd@NCS, **b)** the N1s core level peak

of the PtPd@PDA and PtPd@NCS, **c)** the C1s core level peak of the PtPd@PDA and PtPd@NCS, **d)** the Pt4f core level peak of the PtPd@NCS and **e)** the Pd3d core level peak of the PtPd@NCS

Fig. 4 **a)** CV responses, **b)** Nyquist plots of the bare GCE, PtPd@NCS/GCE, Pt/C/GCE, MPtPdN/GCE, and MCS/GCE in 0.1 M PBS (pH 7.5) containing 5.0 mM of $[Fe(CN)_6]^{3-/4-}$ and 0.1 M KCl at a scan rate of 50 mV/s and **c)** CV responses from the bare GCE, PtPd@NCS/GCE, and AChE/PtPd@NCS/GCE in 0.1 M PBS (pH 7.5) solution containing 1.0 mM of ATCl at a scan rate of 50 mV/s.

Fig. 5 Current-time plot of AChE/PtPd@NCS/GCE in 0.1 M PBS (pH 7.5) at an applied potential of 650 mV with successive injections of ATCl; Inset: calibration curves for ATCl determination

Fig. 6 **a)** DPV of the AChE/PtPd@NCS/GCE in PBS solution with a pH of 7.5 containing 2.0 mM of ATCl after inhibition with malathion for 10 min. Malathion concentrations are as follows: (a-k: 0, 1×10^{-14}, 1×10^{-13}, 1×10^{-12}, 1×10^{-11}, 1×10^{-10}, 1×10^{-9}, 1×10^{-8}, 1×10^{-7}, 1×10^{-6}, and 1×10^{-5} M), and **b)** the relationship between inhibition and malathion concentration., (Error bars denote the standard deviation from three repeated experiments)

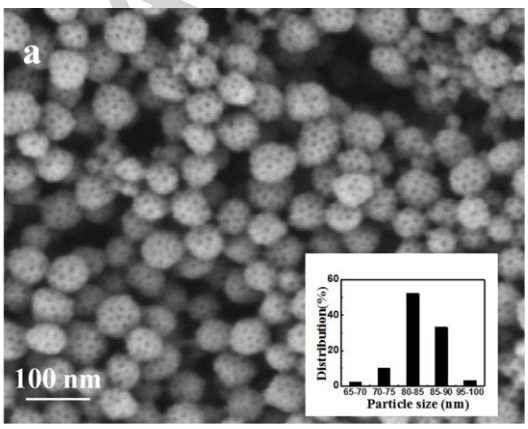

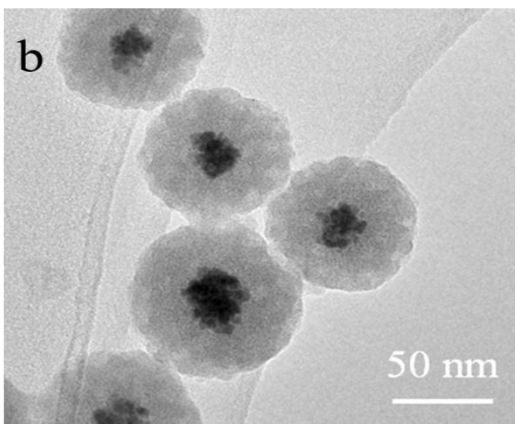

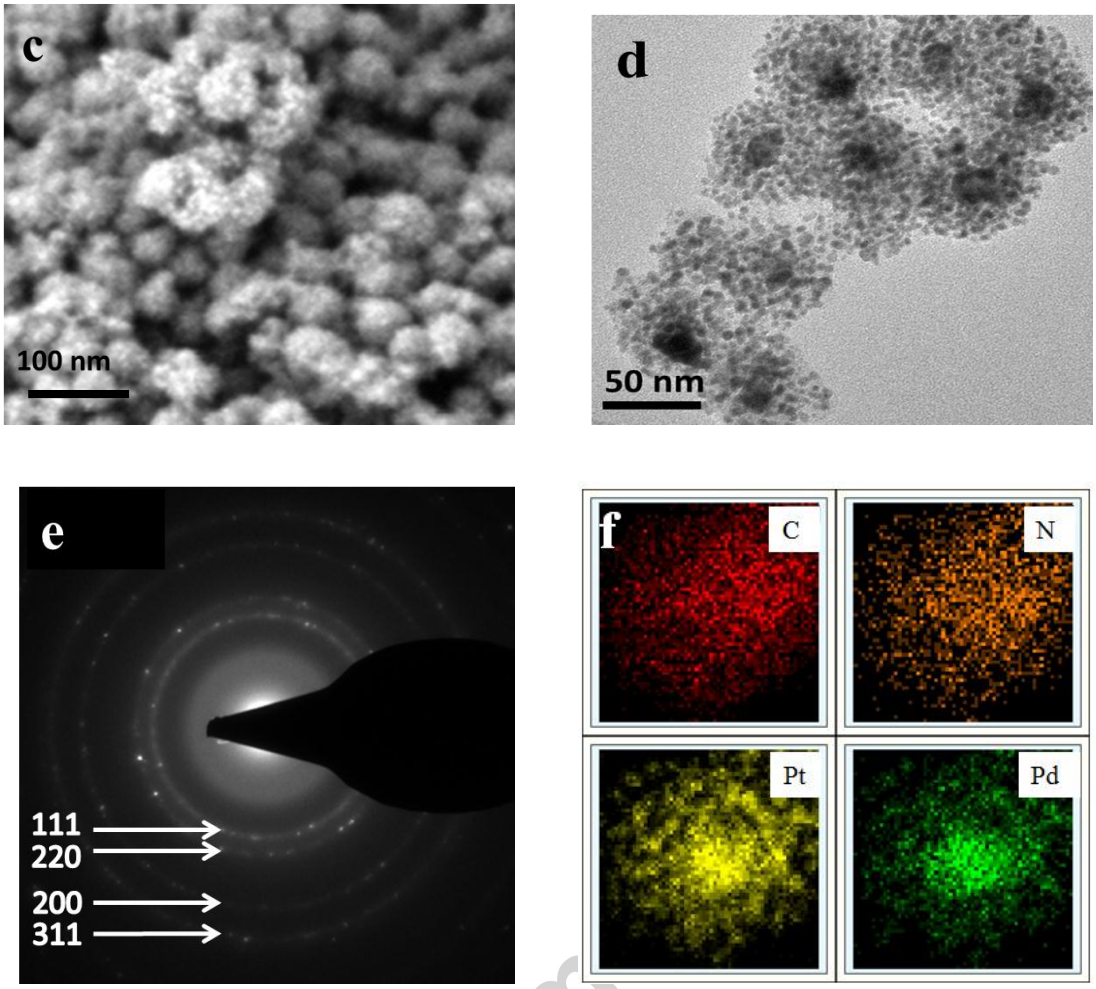

Fig. 1

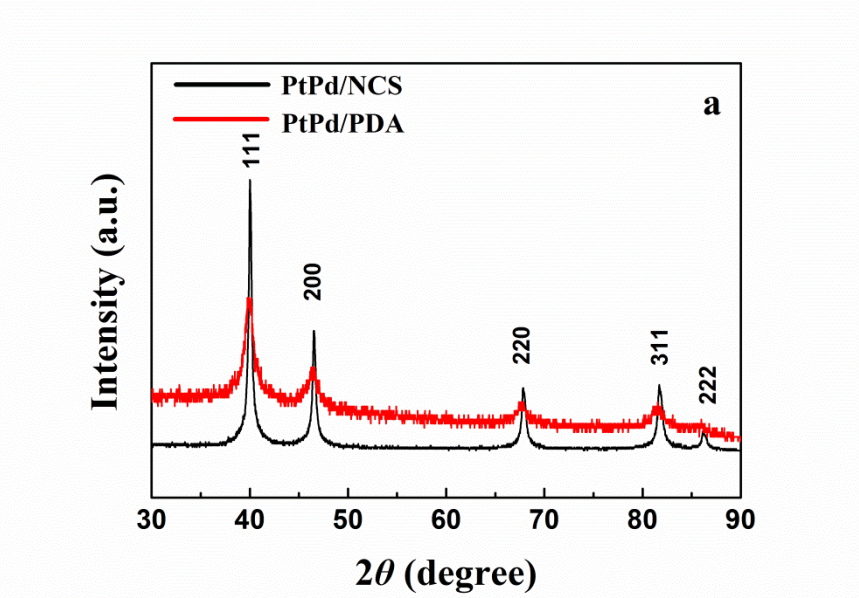
PtPd/NCS
PtPd/PDA
a
111
200
220
311
222
Intensity (a.u.)
30
40
50
60
70
80
90
2θ (degree)

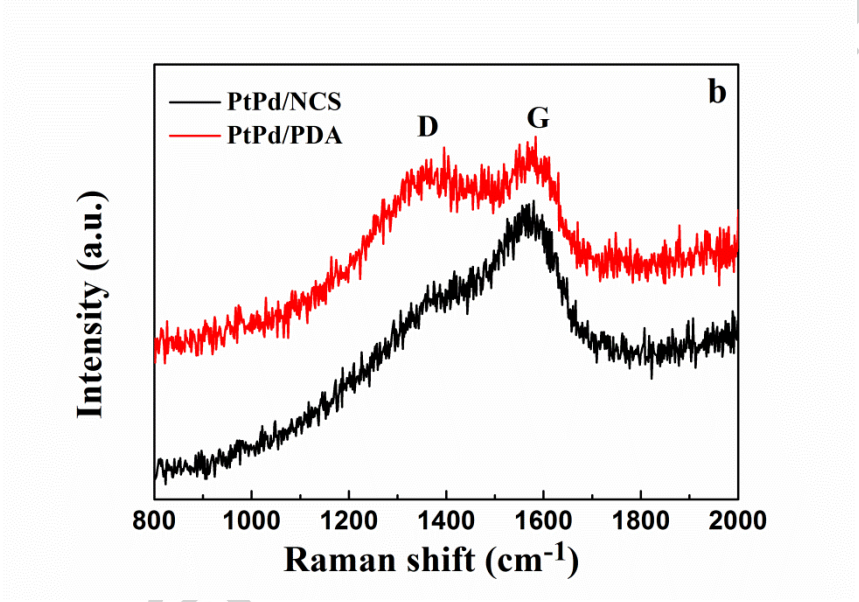
PtPd/NCS
PtPd/PDA
b
D
G
Intensity (a.u.)
800
1000
1200
1400
1600
1800
2000
Raman shift (cm-1)

Fig. 2

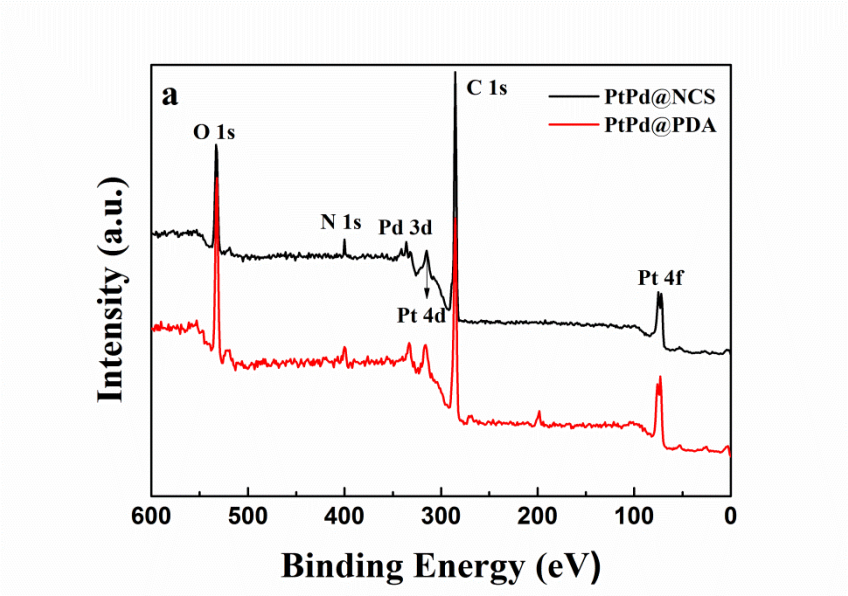

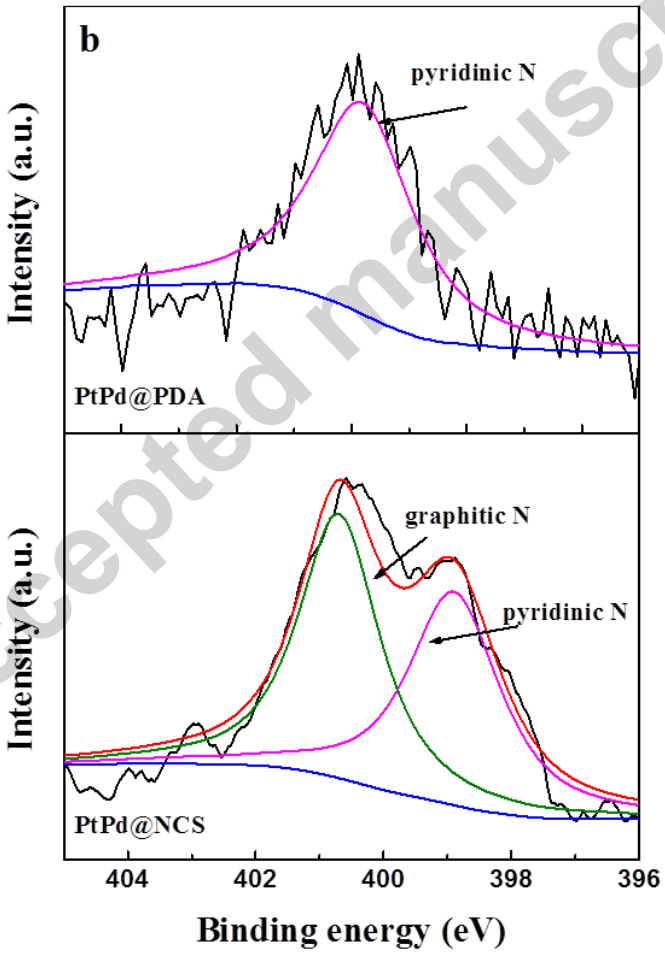

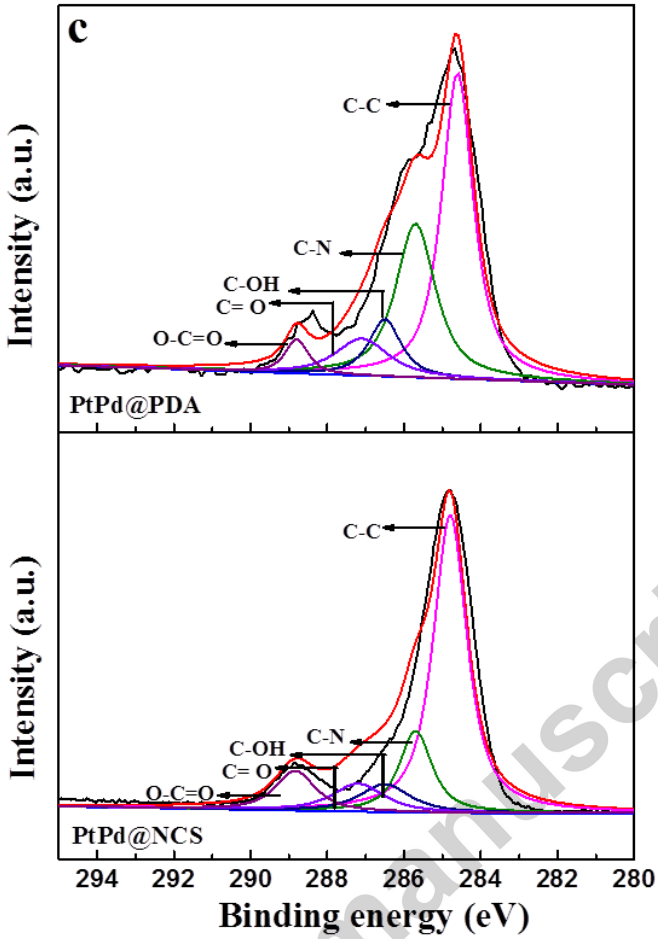

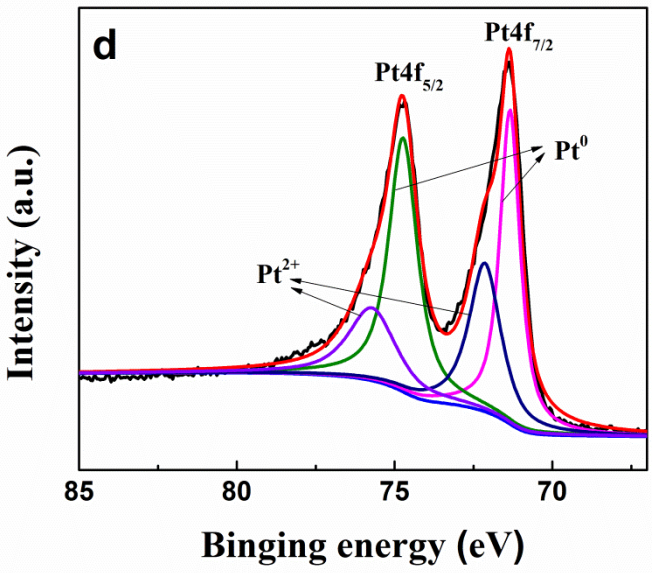

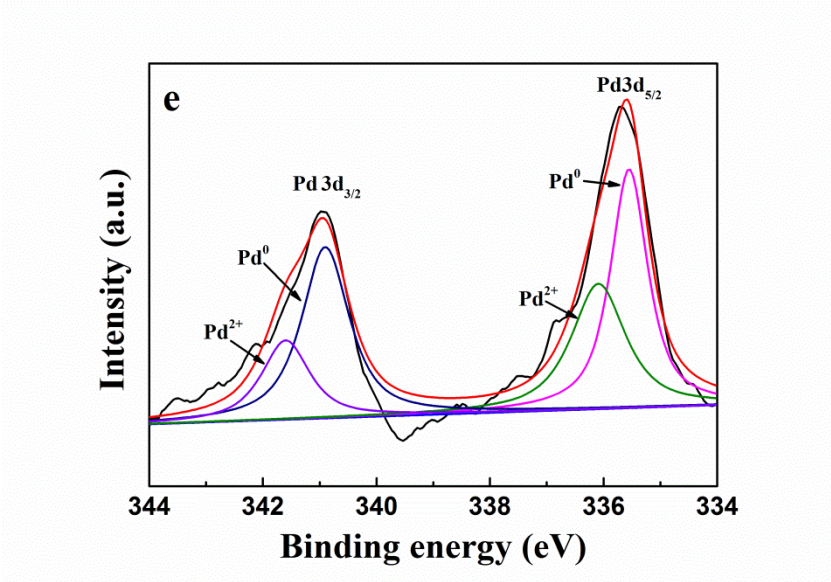
e
Pd3d5/2
Pd 3d3/2
Pd0
Pd0
Pd2+
Pd2+
Intensity (a.u.)
344
342
340
338
336
334
Binding energy (eV)

Fig. 3

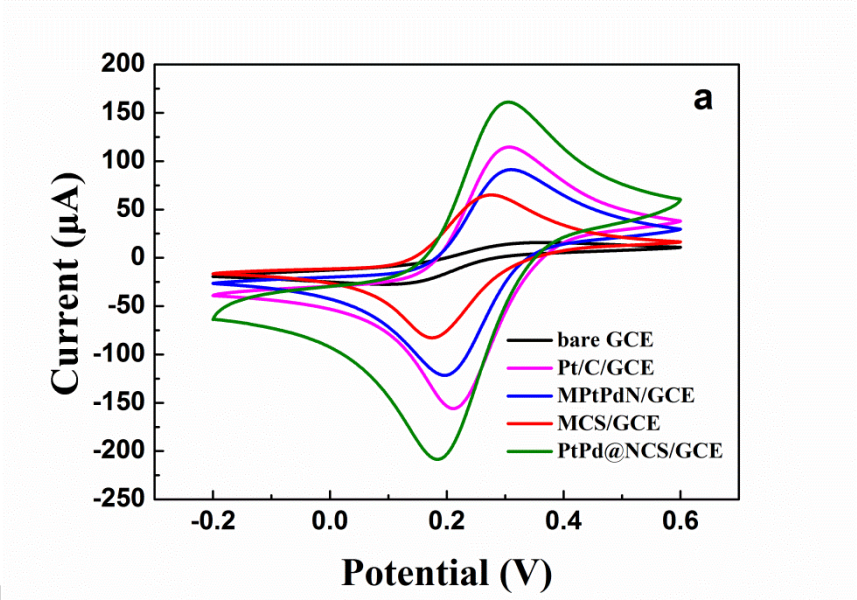
a
200
150
100
50
0
-50
-100
-150
-200
-250
Current (μA)
-0.2
0.0
0.2
0.4
0.6
Potential (V)
bare GCE
Pt/C/GCE
MPtPdN/GCE
MCS/GCE
PtPd@NCS/GCE

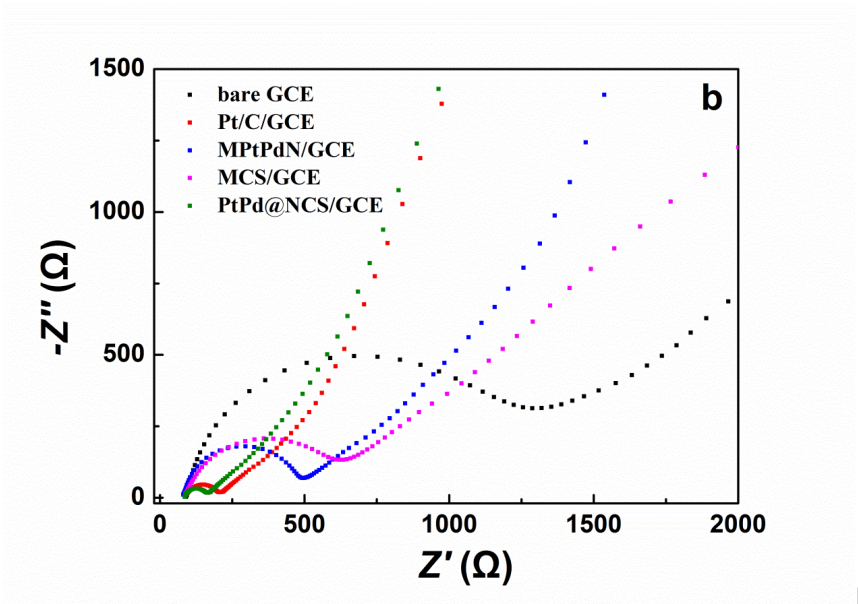
b
bare GCE
Pt/C/GCE
MPtPdN/GCE
MCS/GCE
PtPd@NCS/GCE
-Z'' (Ω)
Z' (Ω)
0
500
1000
1500
2000

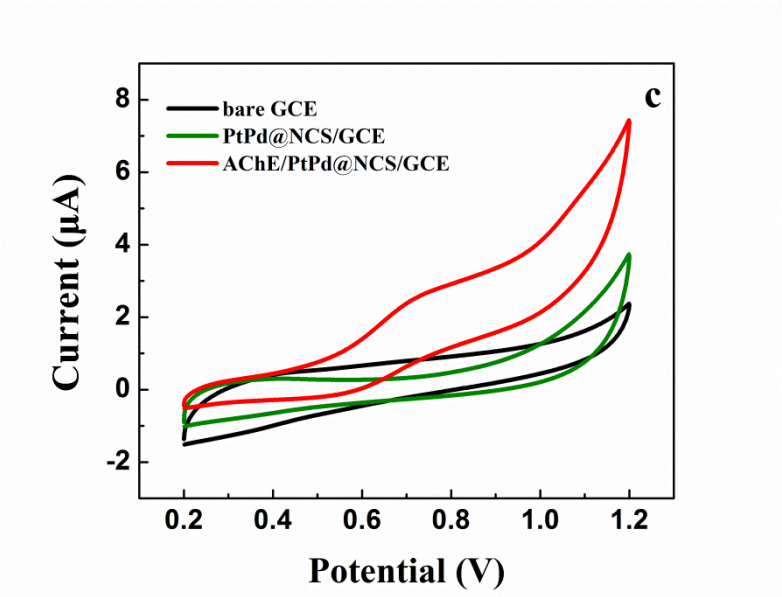
c
bare GCE
PtPd@NCS/GCE
AChE/PtPd@NCS/GCE
Current (μA)
Potential (V)
8
6
4
2
0
-2
0.2
0.4
0.6
0.8
1.0
1.2

Fig.4

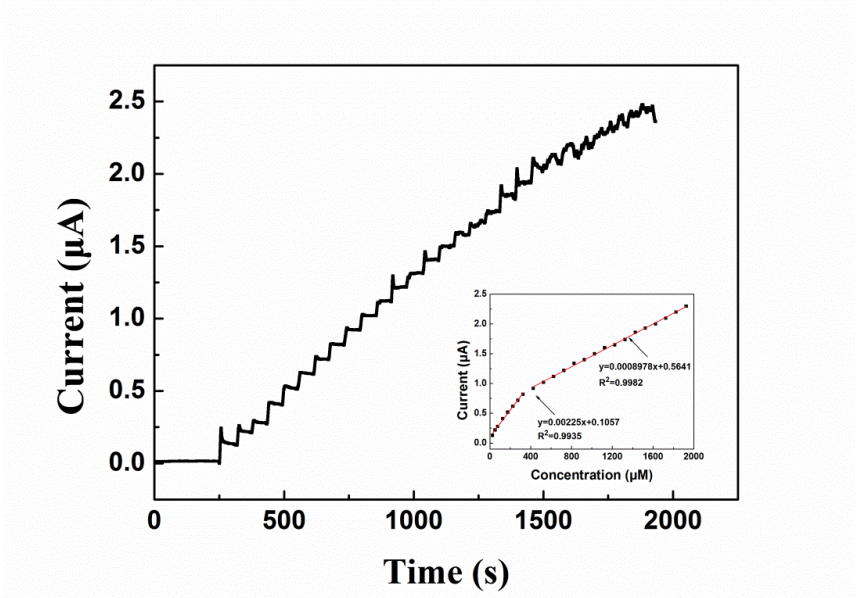
Current (μA)
Time (s)
0
500
1000
1500
2000
0.0
0.5
1.0
1.5
2.0
2.5
Current (μA)
Concentration (μM)
y=0.0008978x+0.5641
R²=0.9982
y=0.00225x+0.1057
R²=0.9935

Fig. 5

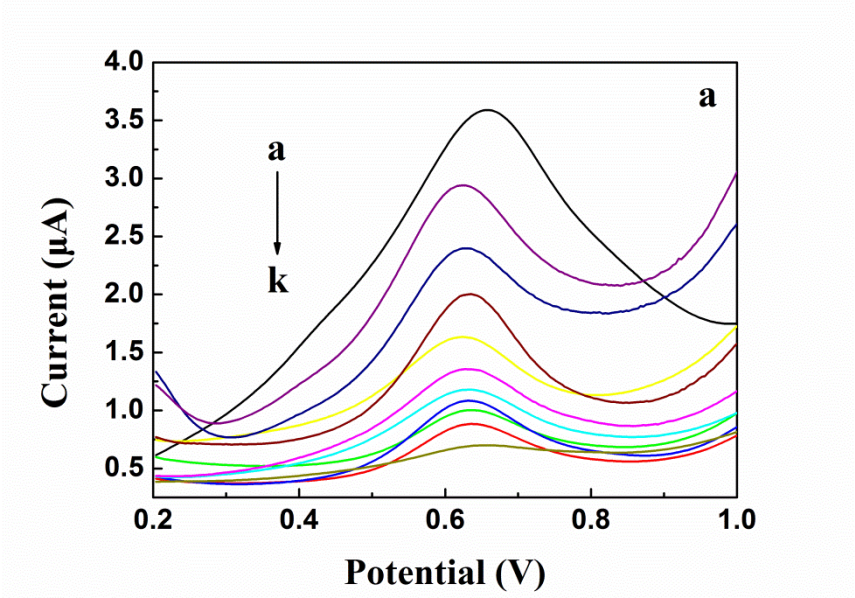
Current (μA)
Potential (V)
a
k
a
0.2
0.4
0.6
0.8
1.0
0.5
1.0
1.5
2.0
2.5
3.0
3.5
4.0

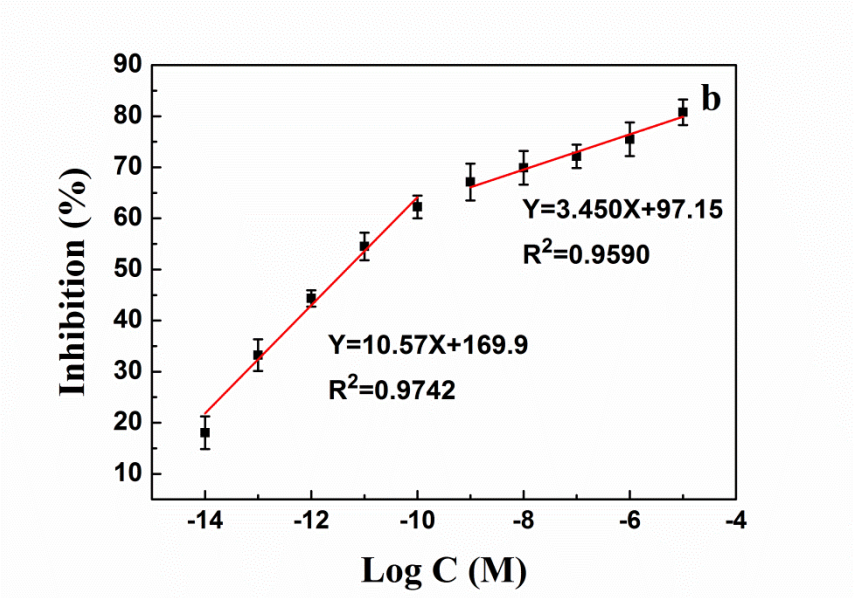

Fig. 6

Highlights

- One-pot approach to fabricate core@shell structured nanocomposites.
- Pt-Pd NPs encapsulated in N-doped carbon shells with a core@shell nanostructure core were synthesized.
- The AChE biosensor was based on the core@shell structured nanocomposites.
- The prepared AChE biosensor was an effective device for detecting OPs.